Ferromagnet/Two-Dimensional Semiconducting Transition-Metal Dichalcogenide Interface with Perpendicular Magnetic Anisotropy

Wen Zhang,[1,‡,] Ping Kwan Johnny Wong,[3,‡] Xiaochao Zhou,[2] Ashutosh Rath,[4] Zhaocong Huang,[2] Hongyu Wang,[4] Simon A. Morton,[5] Jiaren Yuan,[1] Lei Zhang,[1] Rebekah Chua,[6,1] Shengwei Zeng,[1,7] Er Liu,[8] Feng Xu,[8] Ariando,[1,7] Daniel H. C. Chua,[4] Yuan Ping Feng,[1] Gerrit van der Laan,[9] Stephen J. Pennycook,[3,4] Ya Zhai[2,*] and Andrew T. S. Wee[1,3,*]*

[1]Department of Physics, National University of Singapore, 2 Science Drive 3, Singapore 117542, Singapore

[2]School of Physics, Southeast University, Nanjing 211189, China

[3]Centre for Advanced 2D Materials and Graphene Research Centre, National University of Singapore, 6 Science Drive 2, Singapore 117546, Singapore

[4]Department of Materials Science and Engineering, National University of Singapore, Singapore 117575, Singapore

[5]Lawrence Berkeley National Laboratory Berkeley, CA 94720, USA

[*] E-mails: xiaotur@gmail.com, yazhai@seu.edu.cn, phyweets@nus.edu.sg.

[6]NUS Graduate School for Integrative Sciences and Engineering, National University of Singapore, Centre for Life Sciences, #05-01, 28 Medical Drive, 117456 Singapore

[7]NUSSNI-NanoCore, National University of Singapore, 5A Engineering Drive 1, Singapore 117411

[8]School of Materials Science and Engineering, Nanjing University of Science and Technology, Nanjing 210094, China

[9]Magnetic Spectroscopy Group, Diamond Light Source, Didcot OX11 0DE, UK

TOC

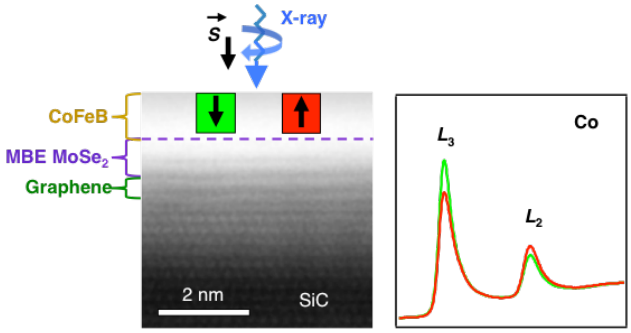

ABSTRACT. Ferromagnet/two-dimensional transition-metal dichalcogenide (FM/2D TMD) interfaces provide attractive opportunities to push magnetic information storage to the atomically thin limit. Existing work has focused on FMs contacted with mechanically exfoliated or chemically-vapor-deposition-grown TMDs, where clean interfaces cannot be guaranteed. Here, we report a reliable way to achieve contamination-free interfaces between ferromagnetic CoFeB and molecular-beam epitaxial $MoSe_2$. We show a spin re-orientation arising from the interface, leading to a perpendicular magnetic anisotropy (PMA), and reveal the CoFeB/2D $MoSe_2$ interface allowing for the PMA development in a broader CoFeB thickness-range than common systems such as CoFeB/MgO. Using X-ray magnetic circular dichroism (XMCD) analysis, we attribute generation of this PMA to interfacial *d-d* hybridization, and deduce a general rule to enhance its magnitude. We also demonstrate favorable magnetic softness and considerable magnetic moment preserved at the interface, and theoretically predict the interfacial band matching for spin filtering. Our work highlights the CoFeB/2D $MoSe_2$ interface as a promising platform for examination of TMD-based spintronic applications and might stimulate further development with other combination of FM/2D TMD interfaces.

KEYWORDS. two-dimensional materials, transition-metal dichalcogenides, spintronics, perpendicular magnetic anisotropy, x-ray magnetic circular dichroism, anisotropic orbital moment, interface

Magnetic interfaces are the building blocks of magnetic sensing and data storage technologies.[1,2] Many desirable effects, such as perpendicular magnetic anisotropy (PMA), spin-to-charge conversion and topologically protected magnetization textures, can be engineered by the interfaces.[3,4] In particular, recent theoretical predictions have triggered interest in hybrid interfaces between 3*d* ferromagnets (FMs) and two-dimensional transition-metal dichalcogenides (2D TMDs).[5,6] This is attributed to the potential of 2D materials in pushing magnetic information storage to the atomically thin limit, their high stability with strong in-plane bonds, as well as their ability to form hybrid interfaces without the need for lattice matching.[7] Other benefits of 2D TMDs include their diversity in elemental composition, attractive electronic band structures, valley (pseudospin), large spin-orbit coupling and broken inversion symmetry, thereby providing attractive opportunities for magnetization manipulation and spin-current generation at customized atomic interfaces.[8,9]

Existing experimental studies have focused exclusively on chemically-vapor-deposition-grown or mechanically exfoliated TMDs, which necessitate breaking vacuum or physical transfer (onto a substrate) prior to FM deposition.[10,11] Such approaches cannot provide an atomically clean interface, which is a key factor for achieving large spin signals.[12,13] For instance, in the so-called 2D magnetic tunnel junctions such as NiFe/MoS_2/NiFe, Fe_3O_4/MoS_2/Fe_3O_4 and Co/MoS_2/NiFe, only moderate tunneling magnetoresistance has been demonstrated so far.[11,14,15] The values are greatly below theoretical expectations, probably limited by interface degradation or oxidation caused by the air/wet processes.[7]

Here, we demonstrate a growth strategy in response to the above issue. Specifically, we utilize ultrahigh-vacuum molecular beam epitaxy (MBE) to obtain an ultraclean and large-scale TMD surface, with a selenium cap that can be conveniently removed by post-annealing at a moderate

temperature (>200ºC). This enables (1) wafer-scale TMDs with full coverage on the substrate, guaranteeing no direct contact between the FM and the substrate, and (2) the subsequent FM deposition without interface contamination. Taking advantage of this growth strategy, we achieve a *clean* FM/2D TMD interface between magnetically soft CoFeB and semiconducting 2D $MoSe_2$, either of which has been exclusively studied for their application potential in magnetic and spin storage.[16-18] Interestingly, we show a spin re-orientation arising from the CoFeB/2D $MoSe_2$ interface, leading to a perpendicular magnetic easy axis. Together with the well-retained magnetic moments and magnetic softness at the CoFeB/2D $MoSe_2$ interface, and theoretically predicted interfacial band matching for spin filtering, our work provides exciting opportunities for layered spintronic devices with atomic-level control of their interface properties and for further miniaturization of next-generation spintronic devices.

RESULTS AND DISCUSSION

Structural and electronic information. Since the 2D $MoSe_2$ surface serves as a crucial growth front for subsequent CoFeB deposition, we used STM/STS to characterize the properties of the epitaxial TMD. The large-scale STM topography image in **Figure 1**a shows a full coverage of monolayer $MoSe_2$ on graphene, and triangular islands as the second layer. This coverage of $MoSe_2$ deposition is intended to prevent any direct contact between CoFeB and the graphene, which could otherwise complicate the present study. In the inset, the line profile indicates that the monolayer height is ~6.6 Å, consistent with the expected thickness for one $MoSe_2$ layer. The semiconducting nature of the $MoSe_2$ is confirmed by STS measurement shown in **Figure 1**b, where the dI/dV spectrum taken on the first monolayer reveals a quasi-particle bandgap of ~2.18 eV, in good agreement with previous reports.[19] The epitaxial growth of $MoSe_2$

on graphene/SiC is confirmed by the cross-sectional high-resolution HAADF-STEM image of the $MoSe_2$/graphene interface shown in **Figure 1**c, taken along the [2-1-10] zone axis of SiC. The close-up view of the interface is displayed in the inset. The STEM image of the Pt/CoFeB/$MoSe_2$ interface of stack 2, with *d*-spacing analysis, is presented in **Figure 1**d, and shows that the CoFeB layer grown on epitaxial $MoSe_2$ is polycrystalline with a body-center-cubic (bcc) structure.

Tunable magnetic anisotropy at the CoFeB/2D $MoSe_2$ interface. In order to determine the magnetically anisotropic behavior at the CoFeB/2D $MoSe_2$ interface, XMCD was performed at normal incidence (N.I., $\gamma = 0^o$) and grazing incidence (G.I., $\gamma = 60^o$) of the X-ray beam, as illustrated in **Figure 2**a. In each case, the applied magnetic field was parallel to the incident X-ray beam. **Figures 2**b-c display the angle-dependent XMCD hysteresis loops of the three stacks, obtained by recording the peak height of the Co L_3 signal at ~778 eV divided by the Co L_2 signal at ~793 eV, as a function of applied magnetic field. All loops feature a narrow hysteresis, as reflected by the tiny coercivity (H_C) in **Figure 2**d, and easy-axis squareness higher than 0.8. Similar to those of other soft-magnetic CoFeB thin layers,[20] the H_C values are all smaller than 0.01 T, indicating that the three stacks are easily magnetized and demagnetized with low hysteresis loss. Such magnetic softness suggests 2D $MoSe_2$ as an alternative buffer material for CoFeB-based magnetic switching devices particularly driven by a low electrical switching current.[21] By comparing the N.I. and G.I. hysteresis loops, we assess the magnetic anisotropy of the stacks, which shows a tunability with different Co:Fe compositional ratio and different CoFeB thickness. For stack 1 and 3, the easy axis of magnetization is in the film plane, with the squareness of the G.I. loop much higher than that of the N.I. counterpart. In contrast, stack 2 has its easy axis tilted out of the film plane, with the squareness of the N.I. loop slightly higher than

that of the G.I. one. This observed PMA in stack 2, although small, is noteworthy, due to the following reasons: (*i*) It is not present in those CoFeB similarly grown on Pt buffer layer (see **Figure S1**). Moreover, the easy-axis redirection arises at the 3-nm-thick CoFeB, suggesting the critical FM thickness (t_{cr}) for achieving PMA in CoFeB/2D $MoSe_2$ is ≥3 nm, more than double the values in common systems such as CoFeB/MgO and CoFeB/Ta (≤1.5 nm).[22-24] Here, t_{cr} is defined as $t_{cr} = -2K_i/K_b$ (where K_i is the interface contribution and K_b is the bulk contribution to the effective magnetic anisotropy energy),[25] above which the PMA will disappear. Hence, the large t_{cr} suggests large interface anisotropy energy and allows for the PMA development in a broad thickness-range of CoFeB grown on epitaxial $MoSe_2$. (*ii*) The traditional approach to engineer PMA is to use noble metals or rare earth with high spin-orbit interaction, such as FM/heavy-metal interfaces and rare-earth/transition-metal alloys.[26,27] This usually enhances magnetic damping constant and strongly reduces spin-diffusion lengths, limiting magnetoresistance and precluding low threshold currents for magnetization reversal in spin-torque magnetic random access memories.[28-30] In this regard, our observed PMA is attractive in a view of maintaining weak spin-orbit coupling, which is reflected by the magnetic softness well preserved in the CoFeB layers grown on 2D $MoSe_2$.

Microscopic origin of the PMA at the CoFeB/2D $MoSe_2$ interface. We provide atomic-level insight into the observed PMA at the CoFeB/2D $MoSe_2$ interface by XMCD analysis. **Figure 3** shows typical XA and XMCD spectra taken at the Co $L_{2,3}$-edges from stack 2, with no sign of oxide formation or interfacial intermixing which would otherwise lead to multiplet features in the spectra.[31,32] This is further verified by the Fe $L_{2,3}$-edge spectra of stack 2, as shown in **Figure S2**, confirming a clean CoFeB/$MoSe_2$ interface as aimed for in this study.

Sum rules analysis. — As shown in **Figure 3**, the XA spectra were taken with parallel (μ^-) and antiparallel (μ^+) alignment of the light helicity with respect to the applied magnetic field, and the XMCD was obtained by (μ^- - μ^+). Atomic magnetic moments (per hole), including the orbital (m_L) and spin (m_S) magnetic moments, can be extracted within the framework of the XMCD sum rules as below,[33]

$$m_L = -\frac{4}{3P}\frac{\int_{L_3+L_2}(\mu^+ - \mu^-)dE}{\int_{L_3+L_2}(\mu^+ + \mu^-)dE} \quad , \qquad (1)$$

$$m_S + m_T = -\frac{1}{P}\frac{6\int_{L_3}(\mu^+ - \mu^-)dE - 4\int_{L_3+L_2}(\mu^+ - \mu^-)dE}{\int_{L_3+L_2}(\mu^+ + \mu^-)dE} \quad , \qquad (2)$$

where P is the X-ray circular polarization, and m_T corresponds to the magnetic spin dipole moment arising from the anisotropy of the atomic charge distribution. The latter is expected to vary with the incidence angles, which may cause an anisotropy in the spin distribution and thus needs to be taken care of when extracting the value of m_S. We first treat the ($m_S + m_T$) as a whole and calculate its value from the XA/XMCD spectra using **eq 2**. The resulting ($m_S + m_T$) value is found to be almost isotropic here, *i.e.*, $(m_S + m_T)_{NI} \approx (m_S + m_T)_{GI}$. Accordingly, the m_T term can be safely ignored in our case,[34] and the orbital-to-spin moment ratio, m_L/m_S, can thus be estimated as

$$m_L / m_S = \frac{1}{3 - 4.5(\frac{p}{q})} \quad , \qquad (3)$$

where p is the integral of the dichroic signal of the L_3 peak alone, and q is the integrated dichroism over both the L_3 and L_2 edges, as marked by the arrows in **Figure 3**. Hereafter, we will focus on discussing the ratio of m_L/m_S, which can be taken as an estimate of m_L but provides more accurate information mainly because (*i*) m_L/m_S is independent of the *d*-band hole density in

CoFeB, degree of X-ray circular polarization and status of magnetization, and (*ii*) m_L/m_S is robust to the XA background subtraction during the sum rules analysis.[35,36]

Anisotropic orbital moment versus magnetic anisotropy energy. — In contrast to m_S, m_L/m_S show a highly anisotropic behavior, as displayed in **Figure 4**a. In particular, the ratio at normal incidence, $m_{L,NI}/m_{S,NI}$, shows a much larger variation with Co:Fe ratio and CoFeB thickness, than that at grazing geometry, $m_{L,GI}/m_{S,GI}$. The m_L/m_S of Fe follows a similar trend, as shown in the inset of **Figure 4**a. This suggests that the perpendicular orbital moment plays an essential role in the anisotropic behavior. The resulting anisotropy of orbital moment is estimated by $\Delta(m_L/m_S) = m_{L,NI}/m_{S,NI} - m_{L,GI}/m_{S,GI}$.[37] As shown in **Figure 4**b and the inset, both stack 1 and 3 have a negative $\Delta(m_L/m_S)$ at Co and Fe, while those for stack 2 have an opposite sign. The magnetic anisotropy energy (MAE) of Co, describing the magnetization tendency to align along specific directions,[38] is also plotted for comparison. The MAE is obtained from the difference between the XMCD hysteresis loops measured at different geometries, using $MAE = \frac{\int_0^{m_L+m_S}(HdM_{NI}-HdM_{GI})}{sin^2 60^\circ}$, where H is the applied magnetic field, and M_{NI} and M_{GI} represent the normalized XMCD signal in the N.I. and G.I. loops, respectively.[39,40] Clearly, the MAE follows a consistent trend with the behavior of $\Delta(m_L/m_S)$, which is qualitatively in agreement with the perturbation-theory model proposed by Bruno, where MAE is given by a term proportional to Δm_L.[41] This suggests that the orbital moment, although small, has the ability to redirect the spin moment into a perpendicular direction due to the spin-orbit coupling. We have also prepared a wedged sample, as shown in **Figure 4**c, with the ~3-nm-thick CoFeB grown on $MoSe_2$ and graphene, respectively. With the circularly polarized X-ray beam spots hitting on the two different parts, the Co hysteresis loops are recorded in **Figure 4**d-e. Obviously, the CoFeB grown on graphene shows an in-plane easy

axis of magnetization, in contrast to that grown on $MoSe_2$, confirming interfacial origin of the small PMA in CoFeB/$MoSe_2$.

Microscopic origin of the interfacial PMA. — The above analysis suggests that the anisotropic orbital moment is responsible for the PMA, which would be caused by (*i*) the broken symmetry of the CoFeB layer as compared with the free layer, and (*ii*) the exchange interaction between CoFeB and $MoSe_2$ at the interface. The symmetry breaking and/or the interfacial hybridization lift the degeneracy of the 3*d* orbitals, leading to an energy splitting between those oriented in plane and those with out-of-plane character.[42] Splitting of the bands gives rise to the anisotropic orbital configuration and in turn the anisotropic orbital moments leading to the PMA.[43,44] Here, both Co($3d^7$) and Fe($3d^6$) have more than half-filled *d*-bands while the Mo^{4+}($4d^1$) has a less than half-filled *d*-band, favoring *d*-*d* hybridization at the interface.[45] Similar hybridization effect might be expected for interfaces with similar FM/2D TMD combinations. For instance, W-based TMDs, such as WSe_2 and WS_2 with a less than half-filled *d*-band of W^{4+} ($5d^0$), could be selected and might lead to even stronger interfacial *d*-*d* hybridization than Mo-based TMDs do. In principle, 3*d* transition metals, including Co, Fe and even Ni could be suitable replacements for CoFeB. However, one has to note probably different growth mode and different magnetic softness from those of CoFeB. In contrast to Mo^{4+}($4d^1$), the Pt ($5d^9$) possesses a more than half-filled *d*-band like Co and Fe, which might not promote a strong interaction with the 3*d* metals. This could account for the absence of an interfacial PMA in the samples grown on Pt.

Estimation of PMA enhancement. — Unveiling the microscopic origin of the PMA allows us to estimate the critical parameters that could improve the magnitude of the PMA, based on spin re-orientation upon (*i*) increase of Co:Fe compositional ratio (from stack 1 to 2) and (*ii*) thickness reduction (from stack 3 to 2). Point (*i*) suggests that the higher Co:Fe ratio favors

PMA. This could be understood as follows: Compared to Co, which is a strong FM with its spin-up *d* band completely filled, Fe is less strongly ferromagnetic with both spin *d*-bands only partially filled, and thus would have an electronic structure and magnetic moment that is more sensitive to compositional changes of the alloy.[46] As shown in **Figure 4**b, the $\Delta(m_L/m_S)$ of Fe shows a strong increase of 0.165, much higher than that of Co (0.097). Combined with the higher value of m_S in Fe (reflected in Table 1), it suggests that Fe carries a much higher MAE enhancement than Co does upon the compositional change. Point (*ii*) indicates that the reduced thickness favors PMA. This can be easily understood, as it is established that lower symmetry upon reduced layer thickness can lead to enhanced orbital anisotropy and in turn enhanced MAE.[47] The shift of the Fermi-level (E_F) position may also play an important role in this enhancement,[48] as happens when the m_S changes from stack 3 to 2, which is reflected in Table 1. The m_L and the resultant MAE, depending strongly on the details of the occupied and unoccupied states near E_F, will change accordingly.[49,50] Based on the above two points, we therefore conclude that to use a high Co:Fe compositional ratio with a low CoFeB thickness might be an advantageous way to enhance the interfacial PMA in CoFeB/2D $MoSe_2$ hybrid structures.

Total magnetic moments at the CoFeB/2D $MoSe_2$ interface. — We show in Table 1 that the CoFeB films grown on $MoSe_2$ possess a comparable magnetic moment to those grown on metal or oxide buffer, topological insulator substrate, *etc*.[51-53] This further suggests that epitaxial $MoSe_2$ is a good candidate as buffer material for CoFeB growth, combined with the controllable interfacial PMA *via* proper Co:Fe compositional ratio and thickness.

Theoretical prediction of interfacial band matching in stack 2. As mentioned above, stack 2 is the most attractive among all three stacks due to the PMA formation, and accordingly we performed theoretical calculations for the electronic band structures of stack 2. **Figure 5**a shows

the complex band (left) and band structure (right) of monolayer $MoSe_2$, where the tunneling probability of electrons is revealed to decay exponentially through the $MoSe_2$. The evanescent states with Δ_1 symmetry, possessing the lowest decay rate, is marked in light green in the left panel. These states have the lowest barrier height, and thus will dominate in the electron tunneling of the FM/$MoSe_2$/FM device. **Figure 5**b shows the spin-polarized band structure of bcc $Co_{76}Fe_4$ (here we make an approximation of $Co_{76}Fe_4 \approx$ Co considering the very low Fe content), and the states matching the Δ_1 symmetry of $MoSe_2$ are labeled. We find that only one spin channel (spin-down state) with Δ_1 symmetry touches the E_F, and it is expected that electron tunneling exhibit a symmetry mismatch for the other spin channel. Specifically, the electron with Δ_1 symmetry in the FMs has the largest transmission when the two FMs are in parallel alignment while very small transmission when they are in antiparallel alignment due to the mismatching of the Δ_1 state in the spin-up channel of the electrodes.[54] Thus, the Δ_1 band of monolayer $MoSe_2$ may act as a Δ_1 symmetry filter for the electron spins of CoFeB, which is akin to the well-known spin-filtering effect of an MgO barrier with Fe or CoFeB,[55] providing an exciting prospect for achieving coherent tunneling effect and in turn considerable tunneling magnetoresistance in the CoFeB/2D $MoSe_2$ heterostructure.[56]

CONCLUSIONS

We have exploited a growth strategy to obtain a *contamination-free* FM/2D TMD interface, with a ferromagnetic CoFeB thin layer sputtered onto MBE grown $MoSe_2$. Angle-dependent XMCD analysis demonstrates a spin re-orientation at the 3-nm-thick-$Co_{76}Fe_4B_{20}$/2D $MoSe_2$ interface, suggesting a larger critical thickness for achieving PMA than those in CoFeB/MgO, CoFeB/Ta, *etc*. and in turn allowing for the development of PMA in a broader FM thickness-

range. By a systematic XMCD sum rules analysis of different compositional ratios and thicknesses of CoFeB at the interface, we reveal that the observed PMA originates from interfacial *d-d* hybridization and more importantly, such a PMA is adjustable and is expected to possess a higher value by increasing the Co:Fe compositional ratio and reducing the CoFeB thickness. Together with the magnetic softness and considerable magnetic moment of the magnetic layer, the possible functionality of spin filtering predicted theoretically and of course the benefits of 2D materials (the ultimately reduced thickness and layer-by-layer control, natural sharp definition of the layers and interfaces, *etc*.), the CoFeB/2D $MoSe_2$ interface offers a promising platform for investigation and realization of technologically relevant magnetic and spintronic devices incorporating 2D TMDs. In particular, the CoFeB/2D $MoSe_2$ interface could be attractive in efficient generation of spin-orbit torques,[57] for the strong spin-orbit coupling and inversion symmetry breaking of monolayer TMD.[58,59] In addition, the monolayer TMDs, such as $MoSe_2$, could also provide an advantageous platform for studying the engineering of spin-orbit torques at the 2D scale, in contrast to the relatively large thickness (~6 nm) required for topological insulators.[60]

METHODS

MBE growth of 2D $MoSe_2$. As first demonstrated by Koma *et al*.[61] and in a number of recent studies,[62,63] MBE has become an increasingly important route to fabricate atomically thin layered TMDs. Compared to other popular growth approaches involving low-vacuum and ambient-based chemical vapor deposition techniques,[64,65] MBE has distinct advantages of possible scaling up to wafer sizes and atomic-level controls over stoichiometry, crystallinity and thickness. In this work, a nitrogen-doped SiC(0001) substrate was first graphitized in ultrahigh vacuum by heating

to 1100ºC, leading to a graphene-terminated surface.[66] 2D $MoSe_2$ was then deposited on the substrate in an in-house-built MBE chamber, with a base pressure of better than 1×10^{-9} mbar. High-purity Mo and Se were co-evaporated from an electron-beam evaporator and a standard Knudsen cell, respectively, with the substrate temperature kept at 500°C and a flux ratio of at least ~1:10. To protect samples from environmental contamination during *ex-situ* transport to other ultrahigh-vacuum measurement chambers, a 20-nm-thick Se cap was deposited onto the sample surface. Prior to subsequent sputter deposition of the CoFeB overlayer, this protective cap was desorbed by annealing at 200°C for 20 minutes.

Sputter deposition of CoFeB. Two CoFeB targets with different stoichiometry, *i.e.*, $Co_{60}Fe_{20}B_{20}$ and $Co_{76}Fe_4B_{20}$, were used in this work. All depositions were performed at room temperature in a magnetron sputtering system with a base pressure of 1.0×10^{-5} Pa, and the sputter conditions were optimized at 0.4 Pa Ar pressure and 20 W DC power, in order to minimize damage to the epitaxial $MoSe_2$ layer. To prevent the CoFeB film from oxidation, a 6-nm-thick Pt film was utilized as a capping layer. After fabrication, all samples were heat treated at 380ºC in vacuum for 1 hour. The general sample structure is, therefore, SiC/graphene/$MoSe_2$/CoFeB/Pt, which we have further categorized, according to the CoFeB composition and thickness, as $Co_{60}Fe_{20}B_{20}$(3 nm) for stack 1, $Co_{76}Fe_4B_{20}$(3 nm) for stack 2, and $Co_{76}Fe_4B_{20}$(6 nm) for stack 3.

Scanning tunneling microscopy/spectroscopy (STM/STS) characterization. STM measurements for 2D $MoSe_2$ were carried out in a multi-chamber ultrahigh-vacuum system housing an Omicron LT-STM interfaced to a Nanonis controller. The base pressure was better than 10^{-10} mbar. A chemically etched tungsten tip was used, and the sample was kept at 77 K during the measurement. STM images were recorded in constant-current mode. For the dI/dV

spectroscopic measurements, the tunneling current was obtained using the lock-in technique with a bias modulation of 40 mV at a frequency of 625 Hz.

X-ray absorption/magnetic circular dichroism (XA/XMCD) measurements. Conventional magnetic characterization tools, such as vibrating sample magnetometry (VSM) and superconducting quantum interference device (SQUID), cannot distinguish the intrinsic magnetic signal of CoFeB from that of the substrate. As shown in **Figure S3**, the $MoSe_2$/graphene/SiC presents hysteresis as well, and in particular, the difference between the in-plane and out-of-plane loops shows a magnetic anisotropy, which would complicate the study. A similar phenomenon has been reported previously,[67] which has led to a controversy on the TMD magnetism, while subtracting the substrate contribution from the VSM/SQUID signal could be very tricky.[68] At this point, synchrotron radiation based XMCD is a perfect tool for investigating the *intrinsic* magnetism from the CoFeB, by selecting the X-rays within the energy range of the absorption edges of specific elements.[69] The Co and Fe $L_{2,3}$ edge XA/XMCD spectra were collected in total-electron-yield mode,[70] where the sample drain current was recorded as a function of photon energy, with fixed helicity of 60% circularly polarized X-rays and opposite magnetic fields up to ±1.5 T. The angle of incidence of the photon beam was set to 0° and 60°, respectively, with respect to the sample normal. After normalization to the incident beam intensity, the XMCD spectrum was obtained as the difference between the two XA spectra measured with opposite magnetization directions. XMCD hysteresis loops were measured by recording the peak heights of the Co L_3 and L_2 XA signals, respectively, as a function of applied magnetic field. Measurements were carried out at room temperature on beamline 6.3.1 at the Advanced Light Source, Berkeley, USA.

Scanning transmission electron microscopy (STEM) analysis. Cross-sectional high-resolution high-angle annular dark-field (HAADF)-STEM was performed using a JEOL JEM-ARM200F microscope equipped with an ASCOR aberration corrector and cold-field emission gun and operated at 200 kV. Electron transparent cross-sectional TEM samples were prepared by *in-situ* lift out using a FEI-VERSA-3d focused-ion beam machine. The HAADF images were acquired with a probe-forming aperture of 30 mrad and collection angle of 68-280 mrad. All HAADF images were filtered by radial Wiener filters to reduce the scanning noise.

ACKNOWLEDGMENTS

We acknowledge financial support from the National Key Research and Development Program of China (2017YFA0204800), the Singapore Ministry of Education Tier 2 grants (MOE2016-T2-2-110), and the National Natural Science Foundation of China (NSFC No. 51571062). Z.C.H. thanks financial support from NSFC (11504047). E.L. thanks financial support from NSFC (51601093) and the Natural Science Foundation of Jiangsu Province (BK20160831). P.K.J.W acknowledges funding support from the National Research Foundation (Medium Sized Centre Programme R-723-000-001-281). S.J.P. acknowledges financial support from NUS. D.C. acknowledges financial support from MOE2016-T2-2-110 and MOE2015-T2-2-041. This research used resources of the Advanced Light Source, which is a DOE Office of Science User Facility under contract no. DE-AC02-05CH11231. The authors would like to acknowledge the Singapore Synchrotron Light Source (SSLS) for providing the facility necessary for conducting the research. The laboratory is a National Research Infrastructure under the National Research Foundation Singapore. We also appreciate valuable discussions with Ping Yang, Zheng Zhang and Jisheng Pan.

FIGURES

Figure 1. STM/STS results for epitaxial MoSe2 grown on graphene, and cross-sectional STEM analysis on the Pt/CoFeB/MoSe2 interface. (a) Large-scale STM image of MoSe2 terraces on graphene. Inset: Line profile indicating the height of monolayer MoSe2 is ~6.6 Å. (b) Spatially averaged STS spectrum indicating the semiconducting character of monolayer $MoSe_2$ with a bandgap of ~2.18 eV. (c) Cross-sectional high-resolution HAADF-STEM image of the $MoSe_2$/graphene interface taken along the [2-1-10] zone axis of SiC and a close up view of the interface (inset) showing the bilayer $MoSe_2$ and bilayer graphene at the interface. (d) Cross-sectional high-resolution HAADF-STEM image of the Pt/CoFeB/$MoSe_2$ interface showing *d*-spacing matching with (220) and (002) planes of bcc CoFeB.

Figure 2. Angle-dependent XMCD hysteresis loops taken at the Co $L_{2,3}$-edges of CoFeB thin layers grown on epitaxial $MoSe_2$. (a) Schematic diagram of the experimental geometry for the XMCD measurements, with the applied magnetic field along the X-ray incidence direction. (b,c) Angle-dependent hysteresis loops taken at normal (N.I., $\gamma = 0^o$, red) and grazing (G.I., $\gamma = 60^o$, blue) incidences, respectively. The two insets display the loops of stack 2 in the same field scale of ±0.2 T, indicating an easy axis pointing along the direction of the surface normal, in contrast to stack 1 and stack 3 where the preferred magnetization is in the film plane. (d) Values of the coercivity (H_C, *i.e.*, the reverse field required to demagnetize the samples after magnetization saturation) obtained from the hysteresis loops.

Figure 3. XA and XMCD spectra of stack 2 taken at the Co $L_{2,3}$ edges for (a) N.I. and (b) G.I., respectively. The spectra are clean, with no sign of multiplet structure, suggesting no intermixing or diffusion at the Pt/CoFeB or CoFeB/$MoSe_2$ interface. The XA spectra were taken with parallel

(μ^-) and antiparallel (μ^+) alignment of the light helicity with respect to the applied magnetic field, and the XMCD was obtained by ($\mu^- - \mu^+$). The pink and aqua lines represent the integrals of the XMCD for N.I. and G.I., respectively. The arrows mark the parameters *p* and *q*, derived from the integral of the dichroic signal.

Figure 4. Anisotropic orbital moment *versus* magnetic anisotropy energy (MAE). (a) The m_L/m_S ratios extracted from Co and Fe (inset, with the same axis labels) *L*-edge XMCD spectra, respectively, for different geometries. (b) Anisotropy of orbital moment, $\Delta(m_L/m_S) = m_{L,NI}/m_{S,NI} - m_{L,GI}/m_{S,GI}$, at Co and Fe (inset, with the same axis labels), respectively, *versus* Co MAE calculated from the angle dependent Co XMCD hysteresis loops. (c) Illustration of step-by-step growth of the CoFeB/$MoSe_2$/graphene/SiC hybrid structure, with the X-ray beam hitting on the areas of the CoFeB/$MoSe_2$ and CoFeB/graphene interfaces, respectively. (d,e) XMCD hysteresis loops, taken at the Co $L_{2,3}$ edges, of the two abovementioned interfaces.

Figure 5. Theoretical calculations for bcc(110)-CoFeB/2D $MoSe_2$ interface. (a) Complex band (left) and band structure (right) of monolayer $MoSe_2$, which is a semiconductor with a direct bandgap. The tunneling probability of electrons decays exponentially through $MoSe_2$. The evanescent states with Δ_1 symmetry, possessing the lowest decay rate, is marked in light green in the left panel. (b) Spin-polarized band structure of bcc $Co_{76}Fe_4$ (here we make an approximation of $Co_{76}Fe_4 \approx$ Co considering the very low Fe content), with the states matching the Δ_1 symmetry of $MoSe_2$ labeled. The Fermi level (E_F) is set to zero.

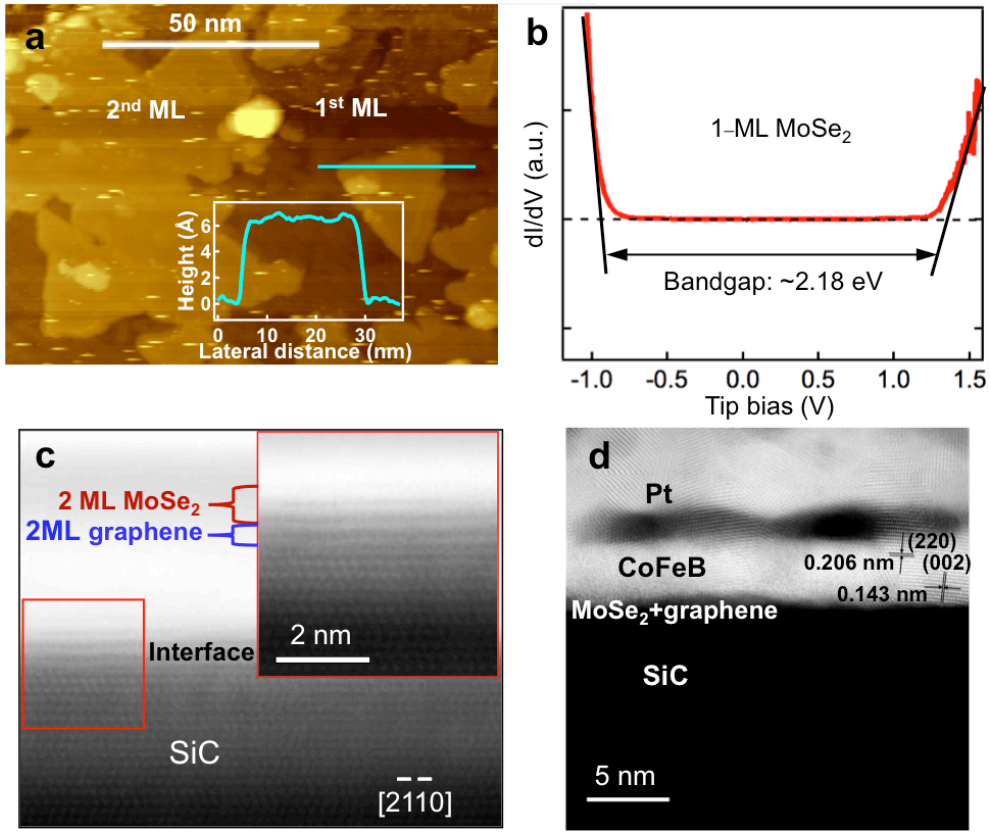
a
50 nm
2nd ML
1st ML
Height (Å)
6
4
2
0
0
10
20
30
Lateral distance (nm)
b
1-ML MoSe2
dI/dV (a.u.)
Bandgap: ~2.18 eV
-1.0
-0.5
0.0
0.5
1.0
1.5
Tip bias (V)
c
2 ML MoSe2
2ML graphene
Interface
2 nm
SiC
[2110]
d
Pt
CoFeB
(220)
0.206 nm
(002)
0.143 nm
MoSe2+graphene
SiC
5 nm

Figure 1

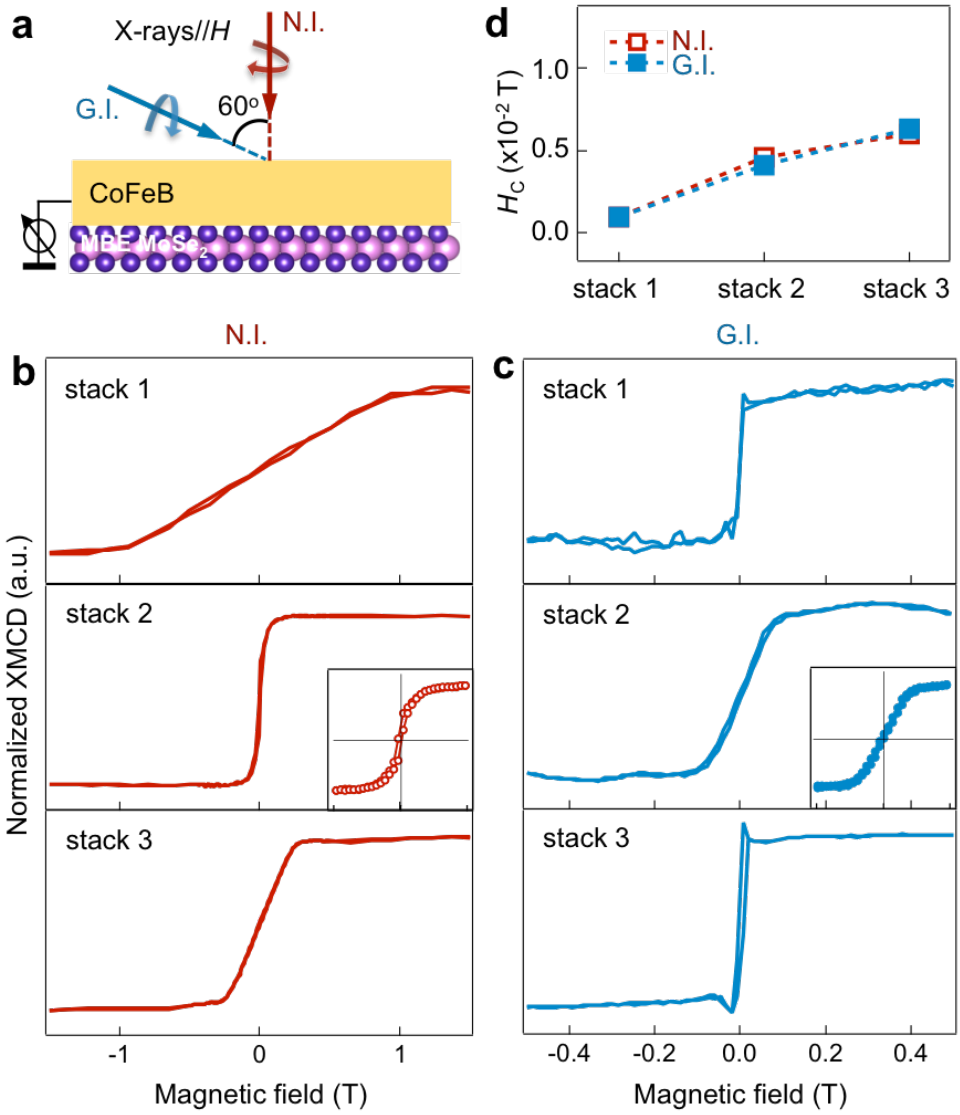
a
X-rays//H
N.I.
G.I.
60°
CoFeB
MBE MoSe2
d
N.I.
G.I.
HC (x10-2 T)
1.0
0.5
0.0
stack 1
stack 2
stack 3
N.I.
G.I.
b
c
stack 1
stack 2
stack 3
Normalized XMCD (a.u.)
-1
0
1
-0.4
-0.2
0.0
0.2
0.4
Magnetic field (T)
Magnetic field (T)

Figure 2

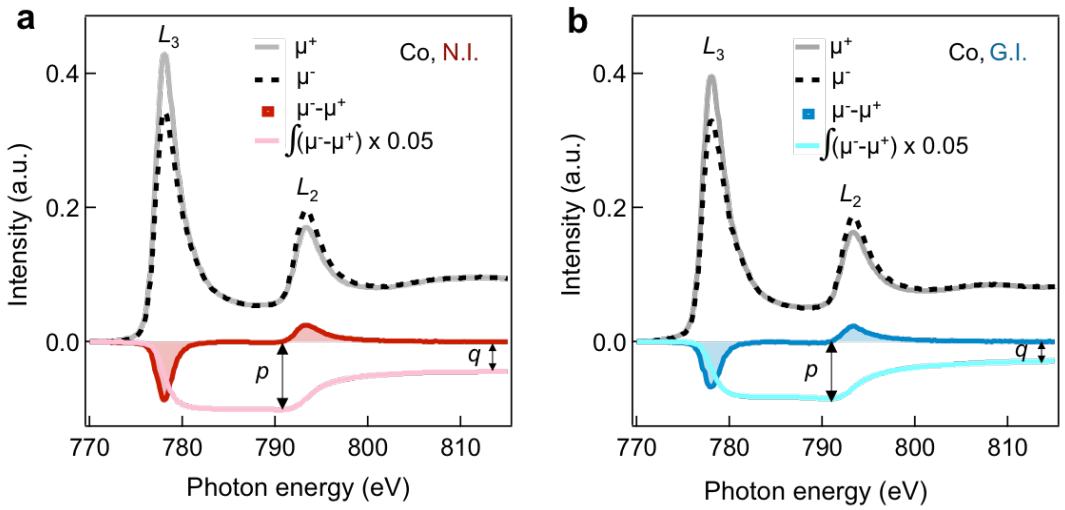
a
b
L_3
L_2
μ⁺
μ⁻
μ⁻-μ⁺
∫(μ⁻-μ⁺) x 0.05
Co, N.I.
Co, G.I.
p
q
Intensity (a.u.)
Photon energy (eV)
0.0
0.2
0.4
770
780
790
800
810

Figure 3

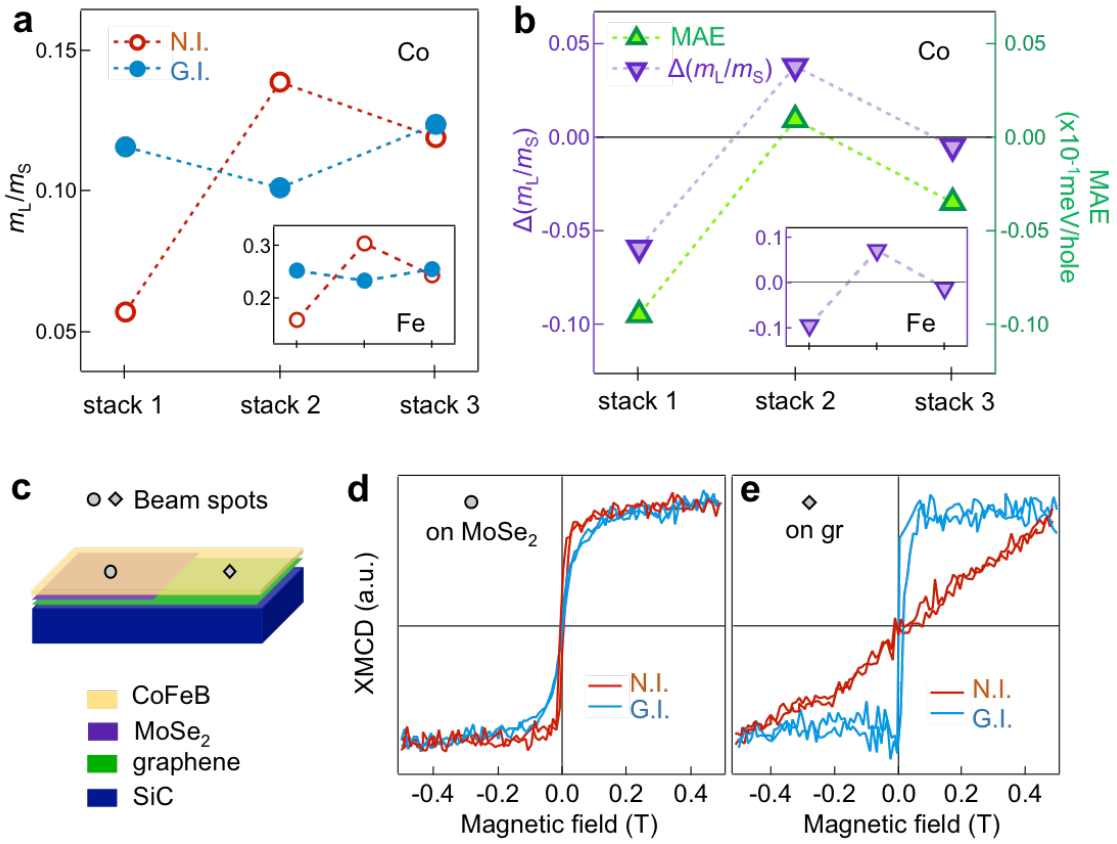
a
N.I.
G.I.
Co
Fe
m_L/m_S
stack 1
stack 2
stack 3
b
MAE
$\Delta(m_L/m_S)$
Co
Fe
$\Delta(m_L/m_S)$
MAE (x10^{-1}meV/hole
stack 1
stack 2
stack 3
c
Beam spots
CoFeB
$MoSe_2$
graphene
SiC
d
on $MoSe_2$
N.I.
G.I.
XMCD (a.u.)
Magnetic field (T)
e
on gr
N.I.
G.I.
Magnetic field (T)

Figure 4

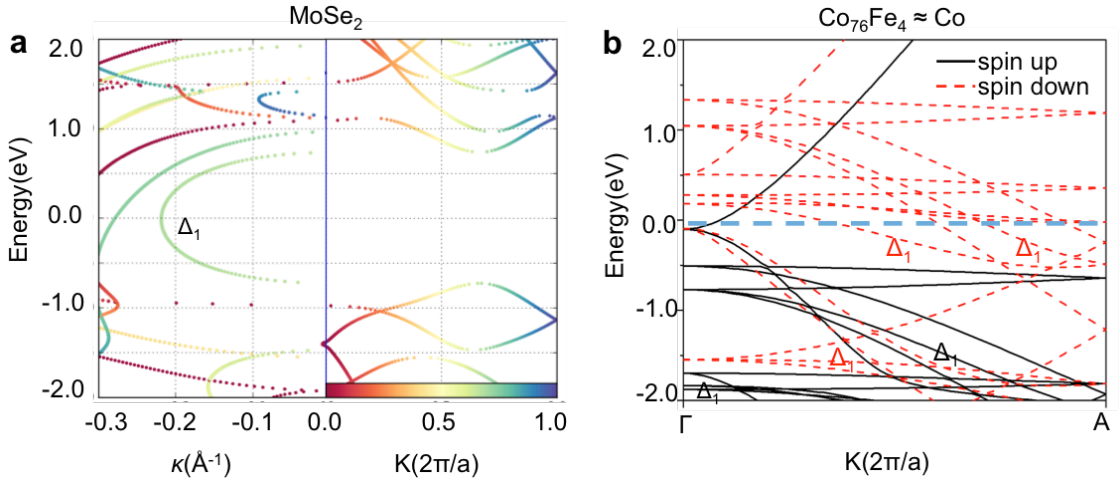
a
MoSe2
2.0
1.0
0.0
-1.0
-2.0
Energy(eV)
Δ1
-0.3
-0.2
-0.1
0.0
0.5
1.0
κ(Å-1)
K(2π/a)
b
Co76Fe4 ≈ Co
spin up
spin down
Δ1
Γ
A
K(2π/a)

Figure 5

TABLES

Table 1. Total magnetic moments, $m_L + m_S$, of Co and Fe extracted from Co and Fe $L_{2,3}$-edge XMCD spectra using the sum rules analysis.

$CoFeB/2D\text{-}MoSe_2$	stack 1: $Co_{60}Fe_{20}B_{20}$ (3 nm)	stack 2: $Co_{76}Fe_4B_{20}$ (3 nm)	stack 3: $Co_{76}Fe_4B_{20}$ (6 nm)
$m_{L,Co} + m_{S,Co}$ (μ_B/hole)	0.40 ± 0.04	0.39 ± 0.04	0.61 ± 0.06
$m_{L,Fe} + m_{S,Fe}$ (μ_B/hole)	0.45 ± 0.05	0.45 ± 0.05	0.71 ± 0.07
References[49]	$Co_{20}Fe_{60}B_{20}$(1.73 nm) on Ta buffer	$Co_{40}Fe_{40}B_{20}$(2 nm) on MgO buffer	$Co_{40}Fe_{40}B_{20}$(5 nm) on Bi_2Te_3 substrate
$m_{L,Co} + m_{S,Co}$ (μ_B/hole)	~ 0.55	0.43	0.56
$m_{L,Fe} + m_{S,Fe}$ (μ_B/hole)	~ 0.57	0.60	0.51

ASSOCIATED CONTENT

Supporting Information Available: XMCD hysteresis loops of CoFeB grown on Pt buffer layer; XA and XMCD spectra of stack 2 taken at the Fe $L_{2,3}$ edges; Details of theoretical calculations; VSM hysteresis loops of $MoSe_2$/graphene/SiC. (PDF) This material is available free of charge *via* the Internet at http://pubs.acs.org.

The authors declare no competing financial interests.

AUTHOR INFORMATION

Corresponding Author

* E-mail: xiaotur@gmail.com.

* E-mail: yazhai@seu.edu.cn.

* E-mail: phyweets@nus.edu.sg.

Author Contributions

‡These authors contributed equally.

REFERENCES

[1] Parkin, S. S. P.; Kaiser, C.; Panchula, A.; Rice, P. M.; Hughes, B.; Samant, M.; Yang, S-H. Giant Tunnelling Magnetoresistance at Room Temperature with MgO (100) Tunnel Barriers. *Nat. Mater.* **2004**, *3*, 862-867.

[2] Baibich, M. N.; Broto, J. M.; Fert, A.; Nguyen Van Dau, F.; Petroff, F.; Etienne, P.; Creuzet, G.; Friederich, A.; Chazelas. J. Giant Magnetoresistance of (001)Fe/(001)Cr Magnetic Superlattices. *Phys. Rev. Lett.* **1988**, *61*, 2472-2475.

[3] Mangin, S.; Ravelosona, D.; Katine, J. A.; Carey, M. J.; Terris, B. D.; Fullerton, E. E. Current-Induced Magnetization Reversal in Nanopillars with Perpendicular Anisotropy. *Nat. Mater.* **2006**, *5*, 210-215.

[4] Soumyanarayanan, A.; Reyren, N.; Fert, A.; Panagopoulos, C. Emergent Phenomena Induced by Spin-Orbit Coupling at Surfaces and Interfaces. *Nature* **2016**, *539*, 509-517.

[5] Dolui, K.; Narayan, A.; Rungger, I.; Sanvito, S. Efficient Spin Injection and Giant Magnetoresistance in Fe/MoS_2/Fe Junctions. *Phys. Rev. B* **2014**, *90*, 041401.

[6] Chen, Q.; Ouyang, Y. X.; Yuan, S. J.; Li, R. Z.; Wang, J. L. Uniformly Wetting Deposition of Co Atoms on MoS_2 Monolayer: A Promising Two-Dimensional Robust Half-Metallic Ferromagnet. *ACS Appl. Mater. Interfaces* **2014**, *6*, 16835-16840.

[7] Piquemal-Banci, M.; Galceran, R.; Martin, M-B.; Godel, F.; Anane, A.; Petroff, F.; Dlubak, B.; Seneor, P. 2D-MTJs: Introducing 2D Materials in Magnetic Tunnel Junctions. *J. Phys. D: Appl. Phys.* **2017**, *50*, 203002.

[8] Xu, X.; Yao, W.; Xiao, D.; Heinz, T. F. Spin and Pseudospins in Layered Transition Metal Dichalcogenides. *Nat. Phys.* **2014**, *10*, 343-350.

[9] Mak, K. F.; McGill, K. L.; Park, J.; McEuen, P. L. The Valley Hall Effect in MoS_2 Transistors. *Science* **2014**, *344*, 1489-1492.

[10] Shao, Q.; Yu, G.; Lan, Y-W.; Shi, Y.; Li, M-Y.; Zheng, C.; Zhu, X.; Li, L-J.; A; Wang, K. L. Strong Rashba-Edelstein Effect-Induced Spin-Orbit Torques in Monolayer Transition Metal Dichalcogenide/Ferromagnet Bilayers. *Nano Lett.* **2016**, *16*, 7514-7520.

[11] Wang, W.; Narayan, A.; Tang, L.; Dolui, K.; Liu, Y.; Yuan, X.; Jin, Y.; Wu, Y.; Rungger, I.; Sanvito, S.; Xiu, F. Spin-Valve Effect in NiFe/MoS_2/NiFe Junctions. *Nano Lett.* **2015**, *15*, 5261-5267.

[12] Yang, T.; Kimura, T.; Otani, Y. Giant Spin-Accumulation Signal and Pure Spin-Current-Induced Reversible Magnetization Switching. *Nat. Phys.* **2008**, *4*, 851-854.

[13] Fukuma, Y.; Wang, L.; Idzuchi, H.; Takahashi, S.; Maekawa, S.; Otani, Y. Giant Enhancement of Spin Accumulation and Long-Distance Spin Precession in Metallic Lateral Spin Valves. *Nat. Mater.* **2011**, *10*, 527-531.

[14] Wong, W. C.; Ng, S. M.; Wong, H. F.; Mak, C. L.; Leung, C. W. Spin-Valve Junction with Transfer-Free MoS_2 Spacer Prepared by Sputtering. *IEEE Trans. Magn.* **2017**, *53*, 1600205.

[15] Dankert, A.; Pashaei, P.; Kamalakar, M. V.; Gaur, A. P. S.; Sahoo, S.; Rungger, I.; Narayan, A.; Dolui, K.; Hoque, Md. A.; Patel, R. S.; de Jong, M. P.; Katiyar, R. S.; Sanvito, S.; Dash, S. P.

Spin-Polarized Tunneling through Chemical Vapor Deposited Multilayer Molybdenum Disulfide. *ACS Nano* **2017**, *11*, 6389-6395.

[16] Kubota, H.; Fukushima, A.; Yakushiji, K.; Nagahama, T.; Yuasa, S.; Ando, K.; Maehara, H.; Nagamine, Y.; Tsunekawa, K.; Djayaprawira, D. D.; Watanabe, N.; Suzuki, Y. Quantitative Measurement of Voltage Dependence of Spin-Transfer Torque in MgO-Based Magnetic Tunnel Junctions. *Nat. Phys.* **2008**, *4*, 37-41.

[17] Wong, P. K. J.; van Geijn, E.; Zhang, W.; Starikov, A. A.; Tran, T. L. A.; Sanderink, J. G. M.; Siekman, M. H.; Brocks, G.; Kelly, P. J.; van der Wiel, W. G.; de Jong, M. P. Crystalline CoFeB/Graphite Interfaces for Carbon Spintronics Fabricated by Solid Phase Epitaxy. *Adv. Funct. Mater.* **2013**, *23*, 4933-4940.

[18] Mak, K. F.; Lee, C.; Hone, J.; Shan, J.; Heinz, T. F. Atomically Thin MoS_2: A New Direct-Gap Semiconductor. *Phys. Rev. Lett.* **2010**, *105*, 136805.

[19] Ugeda, M. M.; Bradley, A. J.; Shi, S-F.; da Jornada, F. H.; Zhang, Y.; Qiu, D. Y.; Ruan, W.; Mo, S-K.; Hussain, Z.; Shen, Z-X.; Wang, F.; Louie, S. G.; Crommie, M. F. Giant Bandgap Renormalization and Excitonic Effects in a Monolayer Transition Metal Dichalcogenide Semiconductor. *Nat. Mater.* **2014**, *13*, 1091-1095.

[20] Fowley, C.; Decorde, N.; Oguz, K.; Rode, K.; Kurt, H.; Coey, J. M. D. Perpendicular Magnetic Anisotropy in CoFeB/Pd Bilayers. *IEEE Trans. Magn.* **2010**, *46*, 2116-2118.

[21] Ikeda, S.; Miura, K.; Yamamoto, H.; Mizunuma, K.; Gan, H. D.; Endo, M.; Kanai, S.; Hayakawa, J.; Matsukura, F.; Ohno, H. A Perpendicular-Anisotropy CoFeB-MgO Magnetic Tunnel Junction. *Nat. Mater.* **2010**, *9*, 721-724.

[22] Johnson, M. T.; Bloemen, P. J. H.; Den Broeder, F. J. A.; De Vries, J. J. Magnetic Anisotropy in Metallic Multilayers. *Rep. Prog. Phys.* **1996**, *59*, 1409-1458.

[23] Gowtham, P. G.; Stiehl, G. M.; Ralph, D. C.; Buhrman, R. A. Thickness-Dependent Magnetoelasticity and its Effects on Perpendicular Magnetic Anisotropy in Ta/CoFeB/MgO Thin Films. *Phys. Rev. B* **2016**, *93*, 024404.

[24] Lu, G.; Huang, X.; Fan, S.; Ling, W.; Liu, M.; Li, J.; Jin, L.; Pan, L. Temperature- and Thickness-Dependent Dynamic Magnetic Properties of Sputtered CoFeB/Ta Bilayer Films. *J. Alloys Compd.* **2018**, *753*, 475-482.

[25] Néel, L. Anisotropie Magnétique Superficielle et Surstructures d'Orientation. *J. Phys. Radium* **1954**, *15*, 225-239.

[26] Mizunuma, K.; Ikeda, S.; Park, J. H.; Yamamoto, H.; Gan, H.; Miura, K.; Hasegawa, H.; Hayakawa, J.; Matsukura, F.; Ohno, H. MgO Barrier-Perpendicular Magnetic Tunnel Junctions with CoFe/Pd Multilayers and Ferromagnetic Insertion Layers. *Appl. Phys. Lett.* **2009**, *95*, 232516.

[27] Emori, S.; Beach, G. S. D. Optimization of Out-of-Plane Magnetized Co/Pt Multilayers with Resistive Buffer Layers. *J. Appl. Phys.* **2011**, *110*, 033919.

[28] Barman, A.; Wang, S.; Hellwig, O.; Berger, A.; Fullerton, E. E.; Schmidt, H. Ultrafast Magnetization Dynamics in High Perpendicular Anisotropy $[Co/Pt]_n$ Multilayers. *J. Appl. Phys.* **2007**, *101*, 09D102.

[29] Slonczewski, J. Current-Driven Excitation of Magnetic Multilayers. *J. Magn. Magn. Mater.* **1996**, *159*, L1-L7.

[30] Berger, L. Emission of Spin Waves by a Magnetic Multilayer Traversed by a Current. *Phys. Rev. B* **1996**, *54*, 9353-9358.

[31] Abrudan, R.; Miguel, J.; Bernien, M.; Tieg, C.; Piantek, M.; Kirschner, J.; Kuch, W. Structural and Magnetic Properties of Epitaxial Fe/CoO Bilayers on Ag(001). *Phys. Rev. B* **2008**, *77*, 014411.

[32] Meng, Y.; Li, J.; Glans, P. -A.; Jenkins, C. A.; Arenholz, E.; Tan, A.; Gibbons, J.; Park, J. S.; Hwang, C.; Zhao, H. Wu.; Qiu, Z. Q. Magnetic Interlayer Coupling between Antiferromagnetic CoO and Ferromagnetic Fe across a Ag Spacer Layer in Epitaxially Grown CoO/Ag/Fe/Ag(001). *Phys. Rev. B* **2012**, *85*, 014425.

[33] Chen, C. T.; Idzerda, Y. U.; Lin, H. -J.; Smith, N. V.; Meigs, G.; Chaban, E.; Ho, G. H.; Pellegrin, E.; Sette, F. Experimental Confirmation of the X-Ray Magnetic Circular Dichroism Sum Rules for Iron and Cobalt. *Phys. Rev. Lett.* **1995**, *75*, 152-155.

[34] Dürr, H. A.; van der Laan, G. Magnetic Circular X-Ray Dichroism in Transverse Geometry: Importance of Noncollinear Ground State Moments. *Phys. Rev. B* **1996**, *54*, R760-R763.

[35] Gambardella, P.; Rusponi, S.; Veronese, M.; Dhesi, S. S.; Grazioli, C.; Dallmeyer, A.; Cabria, I.; Zeller, R.; Dederichs, P. H.; Kern, K.; Carbone, C.; Brune, H. Giant Magnetic Anisotropy of Single Cobalt Atoms and Nanoparticles. *Science* **2003**, *300*, 1130-1133.

[36] Hindmarch, A. T.; Kinane, C. J.; MacKenzie, M.; Chapman, J. N.; Henini, M.; Taylor, D.; Arena, D. A.; Dvorak, J.; Hickey, B. J.; Marrows C. H. Interface Induced Uniaxial Magnetic Anisotropy in Amorphous CoFeB Films on AlGaAs(001). *Phys. Rev. Lett.* **2008**, *100*, 117201.

[37] Stöhr, J.; König, H. Determination of Spin- and Orbital-Moment Anisotropies in Transition Metals by Angle-Dependent X-Ray Magnetic Circular Dichroism. *Phys. Rev. Lett.* **1995**, *75*, 3748-3751.

[38] Chikazumi, S. *Physics of Ferromagnetism*. Clarendon: Oxford, ed. 2, 1997.

[39] Zhang, W.; Morton, S. A.; Wong, P. K. J.; Lu, B.; Xu, Y. B.; de Jong, M. P.; van der Wiel, W. G.; van der Laan, G. Microscopic Origin of the Reduced Magnetocrystalline Anisotropy with Increasing Oxide Content in $Co_{80}Pt_{20}$:Oxide Thin Films. *J. Phys. D: Appl. Phys.* **2013**, *46*, 405001.

[40] Gambardella, P. Dallmeyer, A.; Maiti, K.; Malagoli, M. C.; Rusponi, S.; Ohresser, P.; Eberhardt, W.; Carbone, C.; Kern, K. Oscillatory Magnetic Anisotropy in One-Dimensional Atomic Wires. *Phys. Rev. Lett.* **2004**, *93*, 077203.

[41] Bruno, P. Tight-Binding Approach to the Orbital Magnetic Moment and Magnetocrystalline Anisotropy of Transition-Metal Monolayers. *Phys. Rev. B* **1989**, *39*, 865-868.

[42] Weller, D.; Wu, Y.; Stöhr, J.; Samant, M. G.; Hermsmeier, B. D.; Chappert, C. Orbital Magnetic Moments of Co in Multilayers with Perpendicular Magnetic Anisotropy. *Phys. Rev. B* **1994**, *49*, 12888-12896.

[43] Nakajima, N.; Koide, T.; Shidara, T.; Miyauchi, H.; Fukutani, H.; Fujimori, A.; Iio, K.; Katayama, T.; Nývlt, M.; Suzuki, Y. Perpendicular Magnetic Anisotropy Caused by Interfacial Hybridization *via* Enhanced Orbital Moment in Co/Pt Multilayers: Magnetic Circular X-Ray Dichroism Study. *Phys. Rev. Lett.* **1998**, *81*, 5229-5232.

[44] Ahn, S-M.; Beach, G. S. D. Crossover between In-Plane and Perpendicular Anisotropy in Ta/Co_xFe_{100-x}/MgO Films as a Function of Co Composition. *J. Appl. Phys.* **2013**, *113*, 17C112.

[45] Tyer, R.; van der Laan, G.; Temmerman, W. M.; Szotek, Z.; Ebert, H. Systematic Theoretical Study of the Spin and Orbital Magnetic Moments of 4*d* and 5*d* Interfaces with Fe Films. *Phys. Rev. B* **2003**, *67*, 104409.

[46] Paluskar, P. V.; Lavrijsen, R.; Sicot, M.; Kohlhepp, J. T.; Swagten, H. J. M.; Koopmans, B. Correlation between Magnetism and Spin-Dependent Transport in CoFeB Alloys. *Phys. Rev. Lett.* **2009**, *102*, 016602.

[47] Weller, D.; Stohr, J.; Nakajima, R.; Carl, A.; Samant, M. G.; Chappert, C.; Megy, R.; Beauvillain, P.; Veillet, P.; Held, G. A. Microscopic Origin of Magnetic Anisotropy in Au/Co/Au Probed with X-Ray Magnetic Circular Dichroism. *Phys. Rev. Lett.* **1995**, *75*, 3752-3755.

[48] Wang, D.-S.; Wu, R.; Freeman, A. J. State-Tracking First-Principles Determination of Magnetocrystalline Anisotropy. *Phys. Rev. Lett.* **1993**, *70*, 869-872.

[49] van der Laan, G. Microscopic Origin of Magnetocrystalline Anisotropy in Transition Metal Thin Films. *J. Phys.: Condens. Matter* **1998**, *10*, 3239-3253.

[50] Zhang, W.; Zhang, D.; Wong, P. K. J.; Yuan, H.; Jiang, S.; van der Laan, G.; Zhai, Y.; Lu, Z. Selective Tuning of Gilbert Damping in Spin-Valve Trilayer by Insertion of Rare-Earth Nanolayers. *ACS Appl. Mater. Interfaces* **2015**, *7*, 170170.

[51] Ueno, T.; Sinha, J.; Inami, N.; Takeichi, Y.; Mitani, S.; Ono, K.; Hayashi, M. Enhanced Orbital Magnetic Moments in Magnetic Heterostructures with Interface Perpendicular Magnetic Anisotropy. *Sci. Rep.* **2015**, *5*, 14858.

[52] Cui, B.; Song, C.; Wang, Y. Y.; Yan, W. S.; Zeng, F.; Pan, F. Tuning of Uniaxial Magnetic Anisotropy in Amorphous CoFeB Films. *J. Phys.: Condens. Matter* **2013**, *25*, 106003.

[53] Kaveev, A. K.; Sokolov, N. S.; Suturin, S. M.; Zhiltsov, N. S.; Golyashov, V. A.; Tereshchenko, O. E.; Prosvirin, I. P.; Kokh, K. A.; Sawada, M. Crystalline Structure and XMCD Studies of $Co_{40}Fe_{40}B_{20}$ Grown on Bi_2Te_3, BiTeI and Bi_2Se_3. *arXiv:1801.10061 [cond-mat.mtrl-sci]* **2018**.

[54] Zhang, J.; Zhang, X. -G.; Han, X. F. Spinel Oxides: Δ_1 Spin-Filter Barrier for a Class of Magnetic Tunnel Junctions. *Appl. Phys. Lett.* **2012**, *100*, 222401.

[55] Yuasa, S.; Nagahama, T.; Fukushima, A.; Suzuki, Y.; Ando, K. Giant Room-Temperature Magnetoresistance in Single-Crystal Fe/MgO/Fe Magnetic Tunnel Junctions. *Nat. Mater.* **2004**, *3*, 868-871.

[56] Lee, Y. M.; Hayakawa, J.; Ikeda, S.; Matsukura, F.; Ohno, H. Effect of Electrode Composition on the Tunnel Magnetoresistance of Pseudo-Spin-Valve Magnetic Tunnel Junction with a MgO Tunnel Barrier. *Appl. Phys. Lett.* **2007**, *90*, 212507.

[57] MacNeill, D.; Stiehl, G. M.; Guimaraes, M. H. D.; Buhrman, R. A.; Park, J.; Ralph, D. C. Control of Spin-Orbit Torques through Crystal Symmetry in WTe_2/Ferromagnet Bilayers. *Nat. Phys.* **2017**, *13*, 300-305.

[58] Manchon, A.; Koo, H. C.; Nitta, J.; Frolov, S. M.; Duine, R. A. New Perspectives for Rashba Spin-Orbit Coupling. *Nat. Mater.* **2015**, *14*, 871-882.

[59] Xiao, D.; Liu, G. B.; Feng, W.; Xu, X.; Yao, W. Coupled Spin and Valley Physics in Monolayers of MoS_2 and Other Group-VI Dichalcogenides. *Phys. Rev. Lett.* **2012**, *108*, 196802.

[60] Taskin, A. A.; Sasaki, S.; Segawa, K.; Ando, Y. Manifestation of Topological Protection in Transport Properties of Epitaxial Bi_2Se_3 Thin Films. *Phys. Rev. Lett.* **2012**, *109*, 066803.

[61] Koma, A. Van der Waals Epitaxy — A New Epitaxial Growth Method for a Highly Lattice-Mismatched System. *Thin Solid Films* **1992**, *216*, 72-76.

[62] Zhang, Y.; Chang, T-R.; Zhou, B.; Cui, Y-T.; Yan, H.; Liu, Z.; Schmitt, F.; Lee, J.; Moore, R.; Chen, Y.; Lin, H.; Jeng, H-T.; Mo, S-K.; Hussain, Z.; Bansil, A.; Shen, Z-X. Direct

Observation of the Transition from Indirect to Direct Bandgap in Atomically Thin Epitaxial $MoSe_2$. *Nat. Nanotechnol.* **2014**, *9*, 111-115.

[63] Ugeda, M. M.; Bradley, A. J.; Zhang, Y.; Onishi, S.; Chen, Y.; Ruan, W.; Ojeda-Aristizabal, C.; Ryu, H.; Edmonds, M. T.; Tsai, H-Z.; Riss, A.; Mo, S-K.; Lee, D.; Zettl, A.; Hussain, Z.; Shen, Z-X.; Crommie, M. F. Characterization of Collective Ground States in Single-Layer $NbSe_2$. *Nat. Phys.* **2016**, *12*, 92-97.

[64] Liu, K. K.; Zhang, W.; Lee, Y-H.; Lin, Y-C.; Chang, M-T.; Su, C-Y.; Chang, C-S.; Li, H.; Shi, Y.; Zhang, H.; Lai, C-S.; Li, L-J. Growth of Large-Area and Highly Crystalline MoS_2 Thin Layers on Insulating Substrates. *Nano Lett.* **2012**, *12*, 1538-1544.

[65] Lin, Y. C.; Zhang, W.; Huang, J-K.; Liu, K-K.; Lee, Y-H.; Liang, C-T.; Chu, C-W.; Li, L-J. Wafer-Scale MoS_2 Thin Layers Prepared by MoO_3 Sulfurization. *Nanoscale* **2012**, *4*, 6637-6641.

[66] Huang, H.; Chen, W.; Chen, S.; Wee, A. T. S. Bottom-up Growth of Epitaxial Graphene on 6H-SiC(0001). *ACS Nano* **2008**, *2*, 2513-2518.

[67] Bonilla, M.; Kolekar, S.; Ma, Y.; Diaz, H. C.; Kalappattil, V.; Das, R.; Eggers, T.; Gutierrez, H. R.; Phan, M. -H.; Batzill, M. Strong Room-Temperature Ferromagnetism in VSe2 Monolayers on Van der Waals Substrates. *Nat. Nanotechnol.* **2018**, *13*, 289-293.

[68] O'Hara, D. J.; Zhu, T.; Trout, A. H.; Ahmed, A. S.; Luo, Y. K.; Lee, C. H.; Brenner, M. R.; Rajan, S.; Gupta J. A.; McComb, D. W.; Kawakami, R. K. Room Temperature Intrinsic Ferromagnetism in Epitaxial Manganese Selenide Films in the Monolayer Limit. *Nano Lett.* **2018**, *18*, 3125-3131.

[69] Feng, J.; Biswas, D.; Rajan, A.; Watson, M. D.; Mazzola, F.; Clark, O. J.; Underwood, K.; Markovic, I.; McLaren, M.; Hunter, A.; Burn, D. M.; Duffy, L. B.; Barua, S.; Balakrishnan, G.; Bertran, F.; Le Fèvre, P.; Kim, T. K.; van der Laan, G.; Hesjedal, T.; Wahl, P.; King, P. D. C. Electronic Structure and Enhanced Charge-Density Wave Order of Monolayer VSe_2. *Nano Lett.* **2018**, *18*, 4493-4499.

[70] Zhang, W.; Wong, P. K. J.; Zhang, D.; Yue, J.; Kou, Z.; van der Laan, G.; Scholl, A.; Zheng, J-G.; Lu, Z.; Zhai, Y. XMCD and XMCD-PEEM Studies on Magnetic-Field-Assisted Self-Assembled 1D Nanochains of Spherical Ferrite Particles. *Adv. Funct. Mater.* **2017**, *27*, 1701265.